

ATTRACTION-BASED COMPUTATION OF HYPERBOLIC LAGRANGIAN COHERENT STRUCTURES

DANIEL KARRASCH, MOHAMMAD FARAZMAND, AND GEORGE HALLER

ABSTRACT. Recent advances enable the simultaneous computation of both attracting and repelling families of Lagrangian Coherent Structures (LCS) at the same initial or final time of interest. Obtaining LCS positions at intermediate times, however, has been problematic, because either the repelling or the attracting family is unstable with respect to numerical advection in a given time direction. Here we develop a new approach to compute arbitrary positions of hyperbolic LCS in a numerically robust fashion. Our approach only involves the advection of attracting material surfaces, thereby providing accurate LCS tracking at low computational cost. We illustrate the advantages of this approach on a simple model and on a turbulent velocity data set.

1. INTRODUCTION

Hyperbolic Lagrangian Coherent Structures (LCS) in a two-dimensional unsteady flow are locally most repelling or most attracting material lines over a given finite time interval $I = [t_1, t_2]$ of interest [8]. Both mathematical methods and intuitive diagnostic tools have been developed to locate LCS in finite-time unsteady velocity fields with general time dependence (see [5] for a recent review.)

Most computational approaches to LCS seek their initial or final positions as curves of initial conditions that lead to locally maximal trajectory separation in forward or backward time. This repulsion-based approach requires two numerical runs: one forward-time run that renders the time- t_1 position of forward-repelling LCS, and one backward-time run that reveals the time- t_2 position of forward-attracting LCS. Determining the positions of these material surfaces at an intermediate time t accurately, however, comes at high computational cost: it requires the accurate numerical advection of curves that are unstable in the time direction of advection (see Fig. 1.1, as well as the discussion in [3]).

A recent computational advance is offered by [3], showing how both repelling and attracting LCS can be simultaneously obtained either at t_1 or t_2 from a single numerical run. This approach renders an attracting LCS at a time $t \in [t_1, t_2]$ as the advected image of the initial LCS position at time t_1 . Similarly, the time- t position of a repelling LCS can be obtained by backward-advecting its position from time t_2 to t . Both of these computations track attracting material surfaces, and hence are numerically robust. However, they involve the advection of LCS from two different initial times, and hence are necessarily preceded by two separate numerical advecting of a dense enough grid of initial conditions. Altogether, therefore, the

Date: October 24, 2014.

2010 Mathematics Subject Classification. Primary: 37C60; Secondary: 37N10.

Key words and phrases. Transport, mixing, nonautonomous dynamical systems, Lagrangian Coherent Structures, tracking, stability.

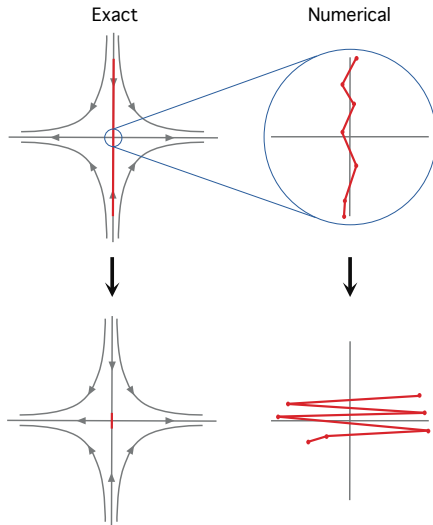


FIGURE 1.1. Forward advection of a classic stable manifold (a repelling LCS over finite times). Inaccuracies in determining the initial location of the LCS lead to exponentially growing errors and accumulation along the unstable manifold even if numerical errors were fully absent in the advection.

computational cost of constructing both repelling and attracting LCS at arbitrary times $t \in [t_1, t_2]$ has remained relatively high.

Here we propose a new computational strategy for two-dimensional incompressible flows. Our strategy builds on results from [3], [9] and [13, 11], enabling the reconstruction of all hyperbolic LCS for arbitrary times $t \in [t_1, t_2]$ in a numerically robust fashion. This approach involves a single integration of trajectories from a full numerical grid, followed by the advection of select attracting material segments from local extrema of the singular value field of the flow gradient. This procedure yields substantial savings in computational time, as well as increased numerical accuracy in LCS detection and tracking. We demonstrate these advantages on a simple analytical flow example and on a direct numerical simulation of two-dimensional turbulence.

This paper is organized as follows. In Section 2, we fix our notation and recall relevant findings from [9] on the singular value decomposition of the linearized flow map. In Section 3 we present our attraction-based approach to hyperbolic LCS in the context of the recent geodesic theory of LCS [6, 2, 1]. In Section 4, we provide a proof of concept in the autonomous Duffing oscillator and compare our approach to previous ones in a simulation of two-dimensional turbulence, before concluding in Section 5.

2. SET-UP

Consider a smooth, two-dimensional vector field $v(x, t)$, defined over a finite interval $I := [t_1, t_2]$ and over spatial locations $x \in D \subset \mathbb{R}^2$. The trajectories

generated by $v(x, t)$ satisfy the ordinary differential equation

$$(2.1) \quad \dot{x} = v(x, t).$$

The t_1 -based flow map is denoted by $F_{t_1}^{t_2}: x_1 \mapsto x_2$, mapping initial values x_1 from time t_1 to their position at time t_2 along the corresponding solution of (2.1). We recall that the flow map is as smooth in x_1 as is v in x .

At any $x_1 \in D$, the *deformation gradient* $DF_{t_1}^{t_2}(x_1)$ is a matrix that admits a singular value decomposition (SVD) of the form

$$(2.2) \quad DF_{t_1}^{t_2} = \Theta \Sigma \Xi^\top, \quad \Theta = (\theta_2 \quad \theta_1), \Xi = (\xi_2 \quad \xi_1) \in O(2), \quad \Sigma = \begin{pmatrix} \sigma_2^f & 0 \\ 0 & \sigma_1^f \end{pmatrix},$$

with $\sigma_2^f \geq \sigma_1^f > 0$ on the flow domain D . The numbers σ_2^f, σ_1^f are the singular values of $DF_{t_1}^{t_2}$; the columns of Ξ (i.e., ξ_2 and ξ_1) are the right singular vectors of $DF_{t_1}^{t_2}$; the columns of Θ (i.e., θ_2 and θ_1) are the left singular vectors of $DF_{t_1}^{t_2}$. From (2.2), we see that

$$DF_{t_1}^{t_2}(x_1) \xi_i(x_1) = \sigma_i^f(x_1) \theta_i(x_2), \quad x_2 = F_{t_1}^{t_2}(x_1), \quad i \in \{1, 2\}.$$

We recall that the singular values $\sigma_2^f(x_1)$ and $\sigma_1^f(x_1)$ measure infinitesimal stretching and compression along the trajectory starting from x_1 . Furthermore, the unit vectors $\xi_2(x_1)$ and $\xi_1(x_1)$ are the tangent vectors pointing to the directions of strongest stretching and compression under the linearized flow $DF_{t_1}^{t_2}(x_1)$.

If the velocity field is incompressible, i.e., $\nabla_x \cdot v(x, t) \equiv 0$, then $\det(DF) = \sigma_1^f \sigma_2^f = 1$, and consequently

$$(2.3) \quad \sigma_2^f = 1/\sigma_1^f.$$

As a result, local maxima of σ_2^f (locally strongest-stretching points) coincide with local minima of σ_1^f (locally strongest-compressing points). At any point $x_1 \in D$, the average exponential rate of largest stretching over the time interval $[t_1, t_2]$ of length $T = t_2 - t_1$ is defined as

$$\Lambda^f(x_1) := \frac{1}{T} \log \sigma_2^f(x_1),$$

which is referred to as the (*forward*) *finite-time Lyapunov exponent* (FTLE). In the incompressible case, Eq. (2.3) shows that the FTLE can equally well be considered as a measure of the strongest local compression at x_1 .

For the backward flow from t_2 to t_1 , the backward deformation gradient is given by

$$(2.4) \quad DF_{t_2}^{t_1}(x_2) = [DF_{t_1}^{t_2}(x_1)]^{-1} = \Xi \Sigma^{-1} \Theta^\top,$$

with $\Sigma^{-1} = \begin{pmatrix} \sigma_1^b & 0 \\ 0 & \sigma_2^b \end{pmatrix} = \begin{pmatrix} 1/\sigma_2^f & 0 \\ 0 & 1/\sigma_1^f \end{pmatrix}$. The singular values of $DF_{t_2}^{t_1}$ are therefore given by

$$(2.5) \quad \sigma_2^b(x_2) = 1/\sigma_1^f(x_1), \quad \sigma_1^b(x_2) = 1/\sigma_2^f(x_1), \quad x_2 = F_{t_1}^{t_2}(x_1),$$

and the backward right singular vectors are given by θ_1 and θ_2 , the strongest- and weakest-stretching directions at x_2 in backward time.¹

Eq. (2.3) shows that the maximal (minimal) singular value of the linearized flow map is equal to the maximal (minimal) singular value of the linearized inverse flow map. Thus, local maxima of σ_2^f are mapped bijectively to local maxima of σ_2^b by

¹The superscripts f and b refer to forward and backward time, respectively.

the flow map. We summarize the equivalences of local extrema of the forward and backward singular value fields as follows:

$$\begin{aligned}
 & x_1 \text{ at } t_1 \xrightarrow{F_{t_1}^{t_2}} x_2 = F_{t_1}^{t_2}(x_1) \text{ at } t_2 \\
 (2.6) \quad & \begin{array}{ccc}
 \sigma_2^f\text{-maximum} & \iff & \sigma_1^b\text{-minimum} \\
 \text{if incompressible} & \Downarrow & \Downarrow \\
 \sigma_1^f\text{-minimum} & \iff & \sigma_2^b\text{-maximum.}
 \end{array}
 \end{aligned}$$

In terms of the backward FTLE field, we recover [7, Prop. 2] for the incompressible case:

$$\Lambda^b(x_2) = \frac{1}{T} \log \sigma_2^b(x_2) = \frac{1}{T} \log (\sigma_1^f(x_1))^{-1} = \frac{1}{T} \log \sigma_2^f(x_1) = \Lambda^f(x_1).$$

In summary, as argued in [9], the SVD of $DF_{t_1}^{t_2}$ yields complete forward and backward stretch information from a uni-directional flow computation.

3. FORWARD AND BACKWARD GEODESIC THEORY OF HYPERBOLIC LCS

The following definition recalls the hyperbolic LCS candidates obtained from two-dimensional geodesic LCS theory.

Definition (Shrink and stretch lines, [2, 3]). We call a smooth curve γ a *forward* (or *backward*) *shrink line*, if it is pointwise tangent to the ξ_1 (or θ_2) field. Similarly, we call γ a *forward* (or *backward*) *stretch line*, if it is pointwise tangent to the ξ_2 (or θ_1) field.

Shrink and stretch lines are solutions of a variational principle put forward in [1] for LCS. This principle stipulates as a necessary condition that the time t_1 positions of hyperbolic LCS must be stationary curves of the averaged Lagrangian shear [1]. This variational principle leads to the result that time t_1 positions of hyperbolic LCS are necessarily null-geodesics of an appropriate Lorentzian metric associated with the deformation field [1]. This prompts us to refer to the underlying approach as geodesic LCS theory.

Away from points where $\sigma_2^f = \sigma_1^f$ at $t = t_1$ and $\sigma_2^b = \sigma_1^b$ at $t = t_2$, both the initial and the final flow configuration is foliated continuously by mutually orthogonal forward and backward shrink and stretch lines. As discussed in [3, 9], the following equivalence relations hold:

$$\begin{aligned}
 & \begin{array}{ccc}
 & \xrightarrow{F_{t_1}^{t_2}} & \\
 \text{at } t_1 & & \text{at } t_2
 \end{array} \\
 (3.1) \quad & \begin{array}{ccc}
 \text{forward shrink line} & \iff & \text{backward stretch line} \\
 \perp & & \perp \\
 \text{forward stretch line} & \iff & \text{backward shrink line.}
 \end{array}
 \end{aligned}$$

The forward shrink and stretch lines provide candidate curves for the positions of repelling and attracting LCS at time t_1 . To find the positions of actual hyperbolic LCS as centerpieces of observed tracer deformation, we seek members of these two line families that evolve into locally most attracting or repelling material lines over the time interval $[t_1, t_2]$.

To this end, we follow [13, 11] to require a sufficient condition that hyperbolic LCS must satisfy. Specifically, the time t_1 positions of *forward repelling LCS* are

shrink lines that intersect local maxima of σ_2^f ; the time t_1 positions of *forward attracting LCS* are stretch lines that intersect local minima of σ_1^f . The time t_2 positions of backward-repelling and backward-attracting LCS are defined analogously using the backward singular-value fields σ_2^b and σ_1^b . By the equivalences detailed above, forward-attracting LCS, as evolving material lines, coincide with backward repelling LCS. Similarly, forward-repelling LCS, as evolving material lines, coincide with backward-attracting LCS.

If the vector field $v(x, t)$ is incompressible, then the relation (2.3) forces local maxima of σ_2^f to coincide with local minima of σ_1^f . As a consequence, both forward-repelling and forward-attracting LCS intersect the maxima of σ_2^f at time t_1 . This fact will simplify our upcoming computational algorithm considerably for incompressible flows.

As noted earlier, reconstructing a full forward-attracting LCS as a material line involves advecting its time t_1 position under the flow map. This is a self-stabilizing numerical process, as it tracks an attracting surface. In contrast, reconstructing a forward-repelling LCS from its time t_1 position by flow advection is an unstable numerical process. Indeed, the smallest initial errors in identifying the LCS position are quickly amplified, as shown in Fig. 1.1.

Relations (2.6) and (3.1), however, allow us to compute the forward-repelling LCS equivalently as backward-attracting LCS. Specifically, forward-repelling LCS positions at a time $t \in [t_1, t_2]$ can be equivalently obtained from advection under the backward flow map $F_{t_2}^t$. The curves to be advected under $F_{t_2}^t$ are just the backward stretch lines running through local minima of σ_1^b . By (2.5), however, local minima of σ_1^b are just the images of local maxima of σ_2^f under the flow map $F_{t_1}^{t_2}$.

The computation of stretch lines still involves the integration of direction fields, for which orientation issues have to be resolved (see [14, 2]). A new feature we introduce here is to advect short line segments (tangents) as opposed to whole stretch lines running through the appropriate extrema of the singular value fields. This idea exploits the tangentially stretching and normally attracting nature of stretch lines, saves on computational cost, and produces highly accurate results, as we demonstrate later. We summarize our attraction-based LCS construction in Fig. 3.1 for the case of incompressible flows. For compressible flows, forward-attracting LCS at time t_1 are still constructed from local minima of σ_1^f , but backward-attracting LCS at t_2 are constructed from advected local maxima of σ_2^f , which generally differ from advected local minima of σ_1^f .

Numerical implementation. Here we summarize the computational steps resulting from our previous considerations, assuming a forward-time advection of the chosen numerical grid.

- (1) **Compute flow map and its linearization:** We solve the ODE (2.1) from a sufficiently dense grid of initial conditions to obtain a discrete approximation to the flow map $F_{t_1}^{t_2}$. We also obtain a numerical approximation to the linearized flow map $DF_{t_1}^{t_2}$ at the grid points by one of four methods: (i) solving the equation of variations associated with (2.1), (ii) finite-differencing $F_{t_1}^{t_2}$ along the grid, (iii) finite-differencing on a smaller auxiliary grid [2], (iv) via convolution with Gaussian kernels [12].
- (2) **Compute singular values:** We compute the singular-value decomposition of the deformation gradient tensor field $DF_{t_1}^{t_2}$. This yields the singular

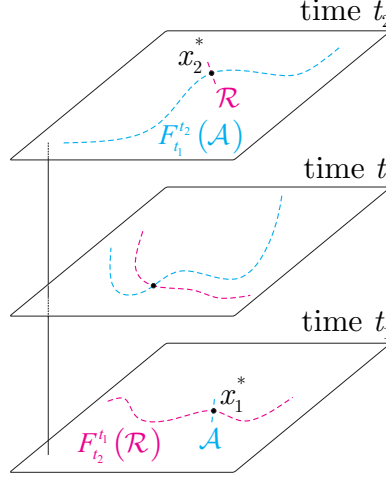


FIGURE 3.1. Illustration of the attraction-based LCS extraction for an incompressible flow at an arbitrary time $t \in [t_1, t_2]$. Here \mathcal{A} denotes a short vector parallel to ξ_2 at a local maximum x_1^* of the $\sigma_2^f(x)$ field. Similarly, \mathcal{R} denotes a short vector parallel to θ_1 at the point $x_2^* = F_{t_1}^{t_2}(x_1^*)$. Recall that both forward-repelling and forward-attracting LCS intersect the maxima of σ_2^f at time t_1 in case of incompressibility.

values σ_i^f as well as the right- and left-singular vector fields ξ_i and θ_i , respectively. The singular values σ_i^b are obtained directly from the relation (2.5).

- (3) **Select seeding points for LCS:** We need to identify points of strongest attraction, i.e. local minima of σ_1^f at the initial time and local minima of σ_1^b at the final time. While the first are identified directly, the latter are advected images of local maxima of σ_2^f under the flow map $F_{t_1}^{t_2}$. In the incompressible case, the points of strongest attraction coincide with local maxima of σ_2^f and their advected images under $F_{t_1}^{t_2}$, respectively. As in [11], we start by sorting all local maxima in ascending order by the values of σ_1^f or descending order by the values of σ_2^f . We then pick the first point p_1 in the ordered list and discard all local extrema in a small neighborhood of p_1 . From the remaining points on the list, we pick the first point p_2 and discard extrema in a small neighborhood of p_2 , and so on. This procedure filters out local extrema in noisy singular value fields.
- (4) **Compute hyperbolic LCS:** For any time $t \in [t_1, t_2]$ of interest, we use the flow map $F_{t_1}^t$ to advect short line segments tangent to $\xi_2(p_i)$ at the points p_i identified in the previous step. The resulting set of curves form the time t positions of attracting LCS. In the incompressible case, we use the flow map $F_{t_2}^t$ to advect short line segments tangent to $\theta_1(F_{t_2}^t(p_i))$ at the points $F_{t_1}^{t_2}(p_i)$. Recall that the characteristic stretching directions for the backward flow are obtained from the forward time computation in step (2) due to Eq. (2.4). The resulting set of curves form the time t positions

of repelling LCS. For the advection of line segments, the use of an adaptive integration scheme may be necessary. This is to fill emerging large gaps between adjacent points due to stretching, and to mitigate the possibly high curvature in the tracked material curve (see, e.g., [10]).

4. EXAMPLES

4.1. Duffing oscillator. We first consider a rescaled version of the unforced, undamped Duffing oscillator with Hamiltonian

$$H(x, y) = \frac{1}{4}x^4 - 2x^2 + \frac{1}{2}y^2.$$

This example has already been used to illustrate shrink and stretch line context by [3] locally around the origin, showing the convergence of forward- and backward maximal stretch directions to the unstable and stable subspaces, respectively. In our present computations, we use the times $t_1 = 0$ and $t_2 = T = 2.5$.

In Fig. 4.1, we compare the results from the earlier numerical LCS detection scheme used in [6] to our approach described in Section 3. While the left plot shows all structures to highlight the homoclinic loop, the middle plot shows that the shrink line deviates from the loop visibly at the first turn. In contrast, the backward-advection line segment stays close to the loop. The right plot shows that at the origin, both the shrink line and the advected stretch line indicate consistently the direction of strongest attraction.

Fig. 4.2 gives further quantitative evidence that the backward-advection backward stretch line gives a better approximation to the actual repelling LCS position at time t_1 than the direct computation of this LCS position from forward shrink lines.

Even in this simple example, therefore, the actual evolution of a shrink line and a backward-advection backward stretch line are noticeable different, although they should theoretically be identical. The root cause is numerical errors in the singular vector computation, as well as the limited ability of the discrete numerical grid to approximate a repelling LCS (local stable manifold) as a continuous curve. The error is initially invisible, but starts to accumulate rapidly during integration of the ξ_2 (θ_1) field and advection.

4.2. Two-dimensional turbulence. As a second example, we consider the two-dimensional Navier–Stokes equations

$$\begin{aligned} \partial_t v + v \cdot \nabla v &= -\nabla p + \nu \Delta v + f, \\ \nabla \cdot v &= 0, \\ v(\cdot, 0) &= v_0, \end{aligned}$$

where the unsteady velocity field $v(x, t)$ is defined on the two-dimensional domain $U = [0, 2\pi] \times [0, 2\pi]$ with doubly periodic boundary conditions. As in [3, 4], we use a standard pseudo-spectral method with 512 modes in each direction, and $2/3$ de-aliasing to solve the above Navier–Stokes equations with viscosity $\nu = 10^{-5}$ on the time interval $[0, 100]$. The flow integration is then carried out over the interval $t \in [50, 100]$, in which the turbulent flow has fully developed, by a fourth-order Runge–Kutta method with variable step-size. The initial condition v_0 is the instantaneous velocity field of a decaying turbulent flow. The external force f is random in phase and band-limited, acting on the wave-numbers $3.5 < k < 4.5$.

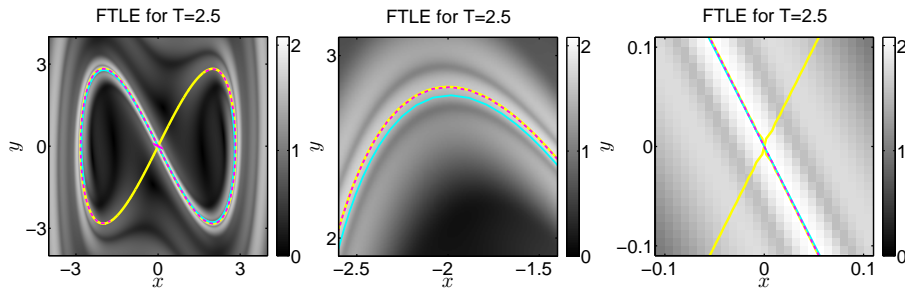


FIGURE 4.1. In the background, the FTLE field for integration time $T = 2.5$ is shown. On top, we show the zero energy level $H = 0$ (yellow), the shrink line (cyan), and a straight line aligned with $\theta_1(0)$ (short line segment not aligned with the homoclinic, magenta) at $t_2 = 2.5$ together with its image at $t_1 = 0$ (magenta). The left figure shows that all structures highlight the homoclinic loop with reasonable accuracy. The magnification in the middle shows, however, a significant deviation of the shrink line from the stable manifold. At the same time, the backward-advected straight line segment approximates the stable manifold perfectly. The right plot shows both the shrink line and the image of the backward stretch line segment to perform well near the origin.

In Fig. 4.3(middle), we plot repelling (red) and attracting (blue) LCS at the middle time instance $t = 75$. As described in Section 3, these LCS were launched as straight line segments of length 0.1 from local σ_2^f -maxima and their flow images, which are σ_2^b -maxima, see Fig. 4.3(left) and (right). The filtering radius for local σ_2^f -maxima was set to 0.2, yielding a reduction from 11,000 to 229 seeding points.

We plot forward shrink lines at the initial time $t_1 = 50$ in Fig. 4.4(left), and compare their forward-advected images (red) at the intermediate time $t = 75$ with the backward advected stretch lines (gray), seeded at the corresponding points (see the middle panel of Fig. 4.4). Analytically, these curves should coincide. In some locations, they indeed agree well, but in other locations, the discrepancy is dramatic (see the close-up view in the right panel of Fig. 4.4). This is the consequence of the effect illustrated in Fig. 1.1, showing the clear advantage of our method over the forward-time tracking of a repelling LCS.

5. CONCLUSIONS

We have proposed a paradigm shift in the detection of hyperbolic Lagrangian Coherent Structures (LCS). Instead of detecting initial positions of LCS as curves of maximal forward repulsion, we seek them as backward-advected locations of maximal backward attraction. While these two approaches are theoretically equivalent, the latter approach (developed here) eliminates an inherent numerical instability of the former approach (used in prior work). We have demonstrated that our

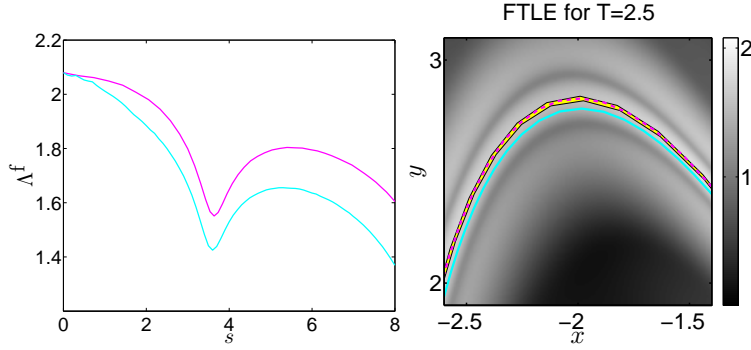


FIGURE 4.2. Left: Comparison of FTLE along the backward-advected backward stretch line (magenta) and the forward shrink line (cyan). Note that the advected stretch line has a uniformly higher repulsion rate and is therefore a better approximation to the repelling LCS. Right: Backward-advected particle blob of initial diameter 1.0 (yellow), backward-advected stretch line (dashed magenta) and forward shrink line (cyan), showing that the advected stretch line is a better approximation to the backward attracting (i.e. repelling) LCS. (The numerical advection is performed by the MATLAB routine `ode45` with absolute and relative error tolerance of 10^{-8} .)

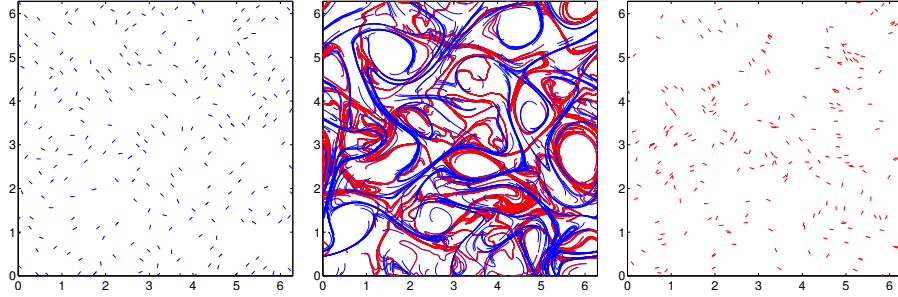


FIGURE 4.3. Attracting (blue) and repelling (red) LCS in a simulation of two-dimensional turbulence over the time interval $[50, 100]$. Left: Initial line segments at $t_1 = 50$ for the attracting LCS. Middle: Hyperbolic LCS positions at $t = 75$. Right: Initial line segments at $t_2 = 100$ for the repelling LCS.

attraction-based approach leads to substantial improvements in accuracy and computational cost.

We have discussed our approach in the framework of the geodesic theory [6, 3, 1], because this theory allows for the explicit computation of hyperbolic LCS as

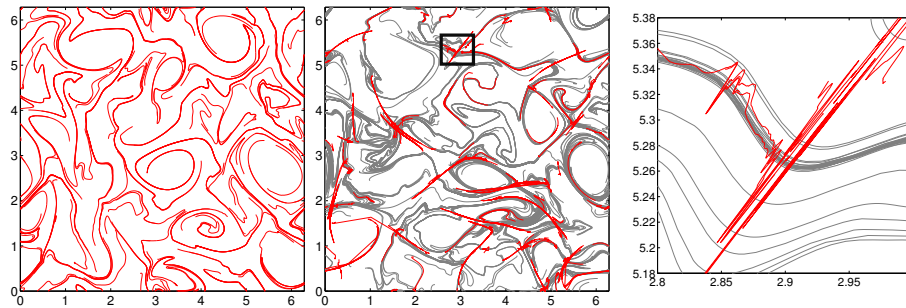


FIGURE 4.4. Left: shrink lines computed directly at $t_1 = 50$ as curves tangent to the $\xi_1(x)$ line field that intersect local maxima of σ_2^f . Middle: the same shrink lines (in red) advected to $t = 75$ to highlight repelling LCS positions at that time. The gray curves are backward-advected stretch lines from $t_2 = 100$ that run through the time t_2 positions of trajectories starting from local maxima of σ_2^f at time t_1 . Right: a close-up view of the middle panel, clearly showing dramatic local inaccuracies from the forward calculation, resembling the effect shown in Fig. 1.1.

parametrized curves. The proposed focus on attraction, however, automatically extends to potential future refinements in LCS computations.

The advection of identified hyperbolic LCS in the stable time direction is a simple idea, but relies heavily on the notion of a forward-time attracting LCS, which has been proposed only recently [3]. We have combined this notion with the SVD of the deformation gradient and with the seeding of straight line segments at points of locally strongest attraction to obtain a dynamically consistent and numerically robust approach to compute LCS. Extensions of these ideas to higher dimensions are possible and will be communicated elsewhere.

REFERENCES

- [1] M. Farazmand, D. Blazevski, and G. Haller. Shearless transport barriers in unsteady two-dimensional flows and maps. *Physica D*, 278-279:44–57, 2014.
- [2] M. Farazmand and G. Haller. Computing Lagrangian coherent structures from their variational theory. *Chaos*, 22(1):013128, 2012.
- [3] M. Farazmand and G. Haller. Attracting and repelling Lagrangian coherent structures from a single computation. *Chaos*, 23(2):023101, 2013.
- [4] M. Farazmand and G. Haller. How coherent are the vortices of two-dimensional turbulence? 2014. submitted preprint.
- [5] G. Haller. Lagrangian Coherent Structures. *Annual Review of Fluid Mechanics*, 2015. to appear.
- [6] G. Haller and F. J. Beron-Vera. Geodesic theory of transport barriers in two-dimensional flows. *Physica D*, 241(20):1680–1702, 2012.
- [7] G. Haller and T. Sapsis. Lagrangian coherent structures and the smallest finite-time Lyapunov exponent. *Chaos*, 21(2):023115, 2011.
- [8] G. Haller and G. Yuan. Lagrangian coherent structures and mixing in two-dimensional turbulence. *Physica D*, 147(3-4):352–370, 2000.

- [9] D. Karrasch. Attracting Lagrangian Coherent Structures on Riemannian manifolds. 2013. submitted.
- [10] A. M. Mancho, D. Small, S. Wiggins, and K. Ide. Computation of stable and unstable manifolds of hyperbolic trajectories in two-dimensional, aperiodically time-dependent vector fields. *Physica D*, 182(3-4):188–222, 2003.
- [11] K. Onu, F. Huhn, and G. Haller. An Algorithmic Introduction to Lagrangian Coherent Structures. in preparation.
- [12] R. Peikert and F. Sadlo. Height Ridge Computation and Filtering for Visualization. In *Visualization Symposium, 2008. PacificVIS '08. IEEE Pacific*, pages 119 –126, 2008.
- [13] B. Schindler, R. Peikert, R. Fuchs, and H. Theisel. Ridge Concepts for the Visualization of Lagrangian Coherent Structures. In R. Peikert, H. Hauser, H. Carr, and R. Fuchs, editors, *Topological Methods in Data Analysis and Visualization II*, Mathematics and Visualization, pages 221–235. Springer, 2012.
- [14] K.-F. Tchon, J. Dompierre, M.-G. Vallet, F. Guibault, and R. Camarero. Two-dimensional metric tensor visualization using pseudo-meshes. *Engineering with Computers*, 22(2):121–131, 2006.

ETH ZÜRICH, INSTITUTE OF MECHANICAL SYSTEMS, LEONHARDSTRASSE 21, 8092 ZÜRICH, SWITZERLAND

E-mail address: `kadaniel@ethz.ch`

ETH ZÜRICH, INSTITUTE OF MECHANICAL SYSTEMS, LEONHARDSTRASSE 21, 8092 ZÜRICH, SWITZERLAND

ETH ZÜRICH, DEPARTMENT OF MATHEMATICS, RÄMISTRASSE 101, 8092 ZÜRICH, SWITZERLAND

E-mail address: `farazmam@ethz.ch`

ETH ZÜRICH, INSTITUTE OF MECHANICAL SYSTEMS, LEONHARDSTRASSE 21, 8092 ZÜRICH, SWITZERLAND

E-mail address: `georgehaller@ethz.ch`